ARTICLE   OPEN

Check for updates

Covalent bonded bilayers from germanene and stanene with topological giant capacitance effects

Binglei Zhang[1,7], Davide Grassano [ID][2,3,7 ✉], Olivia Pulci [ID][3], Yang Liu[1], Yi Luo[1], Adriano Mosca Conte[4], Fedor Vasilievich Kusmartsev [ID][1,5,6] and Anna Kusmartseva[5 ✉]

The discovery of twisted bilayer graphene with tunable superconductivity has diverted great focus at the world of twisted van der Waals heterostructures. Here we propose a paradigm for bilayer materials, where covalent bonding replaces the van der Waals interaction between the layers. On the example of germanene-stanene bilayer, we show that such systems demonstrate fascinating topological properties and manifest giant capacitance effects of the order of $C = 10^2 \mu$ F as well as dipole-like charge densities of $q = 1 - 2 \times 10^{-4} \mu$ C cm^{-2}, showing promise for 2D ferroelectricity. The observed unique behaviour is closely linked to transverse strain-induced buckling deformations at the bilayer/substrate interface. In alternative GeSn bilayer structures with low twist angles the strain distortions trigger rich topological defect physics. We propose that the GeSn bilayer topology may be switched locally by a substrate-strain-induced electric fields. We demonstrate an approach to fabricate covalent bilayer materials, holding vast possibilities to transform applications technologies across solar, energy and optoelectronic sectors.

INTRODUCTION

The discovery of two-dimensional (2D) materials such as graphene[1,2] phosphorene[3–5], silicene[6,7], transition metal dichalcogenides[8,9] has changed our paradigm of nature and revolutionized many of our vital technologies such as opto-electronics and photonics[10,11]. The existence of 2D crystals opens a door to new physics where massless Dirac electrons[12,13] and persistent, topologically protected currents may be observed. Furthermore, by varying the stacking and the combination of the 2D materials it becomes possible to tune the electronic and optical properties[14,15]. In many cases unconventional superconducting and/or insulating phases have been seen[16–22]. Recent discovery of superconducting graphene bilayer with a magic twist angle has confirmed that the relative orientation between the 2D layers plays an equally important role[16–20].

Latest pioneering research using high-level first-principle computations into buckled van der Waals honeycomb bilayers has revealed that such systems are highly susceptible to monolayer stacking configuration within the bilayer[23,24]. Specifically, it was shown in the example of the pristine and mixed arsenene (As) and phosphorene (P) bilayers that by shifting one monolayer with respect to another, the electronic properties of the material may be tuned from a wide bandgap semiconductor to a metal. These studies discovered that buckled honeycomb structures may display diversely rich physics.

To date, the versatility with which van der Waals 2D materials may be influenced has triggered a new innovative era where any desirable material property can be engineered. However, in-depth investigations into covalently bonded bilayers, where the buckling of the bonds naturally promotes interlayer "twisting", are lacking and this field remains completely unexplored until now.

Among the many 2D honeycomb graphene-like materials, stanene and germanene have recently attracted a great deal of attention[13,25–29]. They are composed, respectively, of Sn and Ge atoms, arranged in a single buckled layer due to partial sp^3 hybridization. Their geometry has been experimentally confirmed[30]. Due to the strong buckling, these materials may be fabricated into devices reactive against common air pollution agents such as NO$_x$ and CO$_x$[31]. Both materials have topologically relevant properties, as they are $\mathbb{Z}_2$ insulators[32,33] exhibiting quantum spin Hall effect[34] and displaying dissipationless currents at their edges even at room temperature[35–38].

Electronically, stanene and germanene are massive Dirac systems[26]. Although non-relativistic calculations predict the presence of a gapless Dirac cone at the K point of their Brillouin zone (BZ), the presence of spin-orbit interaction (SOI) opens up a small gap in the spectrum[13,27] (0.024 eV for germanene and 0.075 eV for stanene). However, it was shown that the gap can be closed through the application of a transverse electric field leading to the formation of Dirac cones[39]. Therefore, at a critical value of the electric field both germanene and stanene undergo a topological phase transition from $\mathbb{Z}_2$ to trivial insulators[40–43]. The significant inherent buckling of stanene and germanene as well as their considerable response in an electric field make them ideal candidates for a covalent bilayer heterostructure. Notably, as was shown in recent computational studies germanene and stanene can be combined into inversion-asymmetric topological insulators, such as X2-GeSn monolayers (X= H, F, Cl, Br and I), which demonstrate protected edge states—ideal for dissipationless transport and may be tuned by lattice strain and expansion[44].

Consequently, here we design, fabricate and describe a GeSn bilayer consisting of germanene and stanene covalently bonded to each other. The resulting 2D material demonstrates very

[1]Microsystem and Terahertz Research Center, 610200 Chengdu, P.R. China. [2]Theory and Simulation of Materials (THEOS), École Polytechnique Federale de Lausanne, 1015 Lausanne, Switzerland. [3]Dept. of Physics, and INFN, University of Rome Tor Vergata, Via della Ricerca Scientifica 1, I-00133 Rome, Italy. [4]Istituto dei Sistemi Complessi, Consiglio Nazionale delle Ricerche, Unit Sapienza, Piazzale Aldo Moro 5, 00185 Rome, Italy. [5]Department of Physics, Loughborough University, Loughborough LE11 3TU, UK. [6]College of Art and Science, Khalifa University, PO Box 127788, Abu Dhabi, UAE. [7]These authors contributed equally: Binglei Zhang, Davide Grassano. ✉email: davide.grassano@epfl.ch; A.Kusmartseva@lboro.ac.uk

unusual properties spanning from ferroelectricity to giant capacitance, with non-trivial topological states.

RESULTS

Ab-initio geometry and electronic band structure

Our ab-initio simulations (for details of the method see the section "Ab-initio calculations") show that a surprising crystal structure may arise, with an hexagonal unit cell consisting of 14 atoms (8 Ge and 6 Sn). Germanene and stanene layers are effectively forming an incommensurate structure composed of a 2D unit cell of Ge with 2×2 symmetry and another unit cell of Sn with $\sqrt{3} \times \sqrt{3}$ symmetry. The bilayer unit cell is formed with the help of a twist angle of 30° resulting in a strain of 0.09%. This value was obtained by the coincidence lattice method[45]. The relaxed geometrical structure possesses four local energy minima, the most stable of which, displayed in Fig. 1a and b, is 0.05 eV/atom lower in energy.

The stability of the GeSn bilayer is confirmed by its negative stacking energy $E_{stack} = -0.16$ eV per atom. This value was obtained by comparing the total energy of GeSn with those of the two ideal free-standing monolayers. The top view of the GeSn with 30° twist angle is displayed in Fig. 1a and shows that the honeycomb structure of the two layers survives. The side view in Fig. 1b instead reveals that the Sn and Ge layers are significantly deformed compared to their corresponding ideal free-standing geometries.

Notably, within the GeSn bilayer the average distance between two first neighbour Ge (Sn) atoms increases from 2.46 Å (2.90 Å) to 2.55 Å (2.95 Å), respectively. The lattice distortions are especially strong for the Sn atoms along the z direction (Fig. 1b). The buckling also increases considerably (see Supplementary Table 1), resulting in a total bilayer thickness of about 6 Å. These geometrical deformations are a direct consequence of the covalent nature of the germanene-stanene interaction.
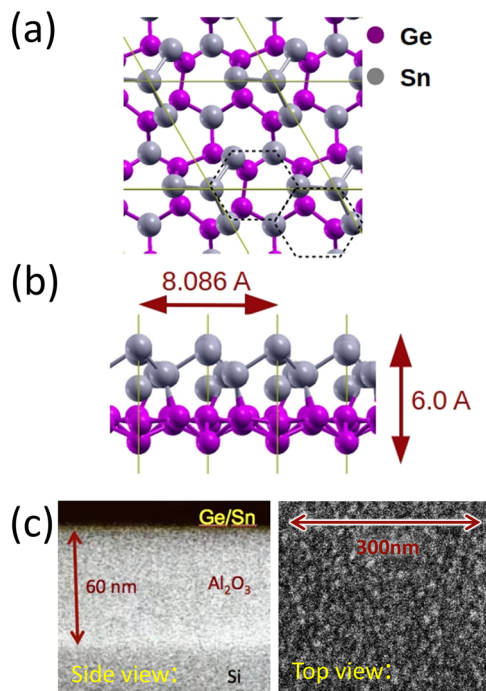
Fig. 1 Theoretical geometry and SEM image. a top-view of the theoretical geometrical structure of free-standing GeSn bilayer. **b** Side view of the relaxed theoretical geometrical structure of free-standing GeSn bilayer. **c** Side-view and top-view SEM images of the GeSn bilayer deposited on a 60 nm thick Al_2O_3 layer, which was grown on a n-doped Si wafer.

The electronic structure of the GeSn bilayer is shown in Fig. 2a. The bands of a free-standing bilayer are highly degenerate both in Γ and K points and, in the proximity of the latter, are reminiscent of the *combined* germanene and stanene Dirac cones. The bandgap is significantly larger (0.10 eV) than that of the single layers and is present even without the SOI. The existence of the bandgap at K is due to the strong interaction between Ge and Sn layers that induces vertical displacements of their atoms as well as a reduction of the symmetry of the individual layers. Note that in spite of these vertical atomic displacements the 2D GeSn unit cell keeps its high symmetry in the plane. The Fermi velocity is about 0.47×10^6 m s^{-1}, a value in between the free-standing germanene and stanene Fermi velocities. The bands near the electronic gap are formed predominantly by Sn p orbitals (55% for occupied bands and 42% for unoccupied ones), while the contribution of the Ge p orbitals is less significant (38% for occupied and 28% for unoccupied bands). The plot of the lowest unoccupied and highest occupied bands in the irreducible Brillouin zone (IBZ) shows a direct electronic gap at K and no other Dirac cones (see Fig. 2b, c).

Individually, germanene and stanene are both $\mathbb{Z}_2$ topological insulators, and undergo a transition to a trivial insulator in an applied external electric field orthogonal to the plane[40,46]. Their ground state band structure is shown in Supplementary Figs. 3, 4. In contrast, according to our ab-initio calculations, the GeSn bilayer appears to be a trivial insulator. Therefore, by combining the Ge and Sn monolayers into a GeSn bilayer, the topological character of the system is reversed. In order to test if band inversion and hence a topological transition, can be achieved in the GeSn bilayer, we apply a constant electric field perpendicular to the material plane, by adding a saw-tooth potential to the Hamiltonian. We observe, by increasing the intensity of the electric field, a closing of the gap at K, however, before a topological transition could be observed, the material switches from an insulator to a metal, due to conduction bands at Γ dropping below the Fermi level (see Supplementary Fig. 5). A possible way to recover the topological transition in this material would be to pin the bands at the Γ k-point by making use of the interaction with a substrate. A discussion of the effect of the substrate on the bilayer is given in Sec. "Possible origin of transverse electric field in GeSn bilayer".

### k · p-model and topological transformation

We have developed and applied the k · p-model to investigate the possible topological phase transformations in the GeSn bilayer under the influence of an applied electric field. The details of the methodology are described in the section "k · p-model". Initially, we consider the electron spectrum of the Hamiltonian described by Eq. (8) for the case when $d = 0$. The K valley spectrum will depend on the charge transfer gap m and the coupling constant q:

$$E(k_x, k_y) = \frac{1}{2}\left(+q \pm \sqrt{4k^2 + (m-q)^2}\right),$$
$$E(k_x, k_y) = \frac{1}{2}\left(-q \pm \sqrt{4k^2 + (m+q)^2}\right) \tag{1}$$

Eqs. (1) indicate an entire range of parameters that define a gapless system satisfying the condition $-|q| < m < |q|$. Outside of this range, a gap $\Delta = |m| - |q|$ will open up (see Fig. 3a)).

Analyzing a sequence of band structures for fixed q, $q \sim m$, and/ or varying m within this model shows the presence of non-trivial topological states (see Fig. 3b)). A Taylor expansion in k around $k = 0$ of Eqs. (1) demonstrates a parabolic band. By applying an electric field E_z, or by varying m, the parabolicity of this band can be switched in sign, leading to a hole-to-electron band transformation. The hole and electron bands are topologically inequivalent, leading to the definition of a topologically non-trivial state in GeSn bilayer that can be tuned by an applied electric field.
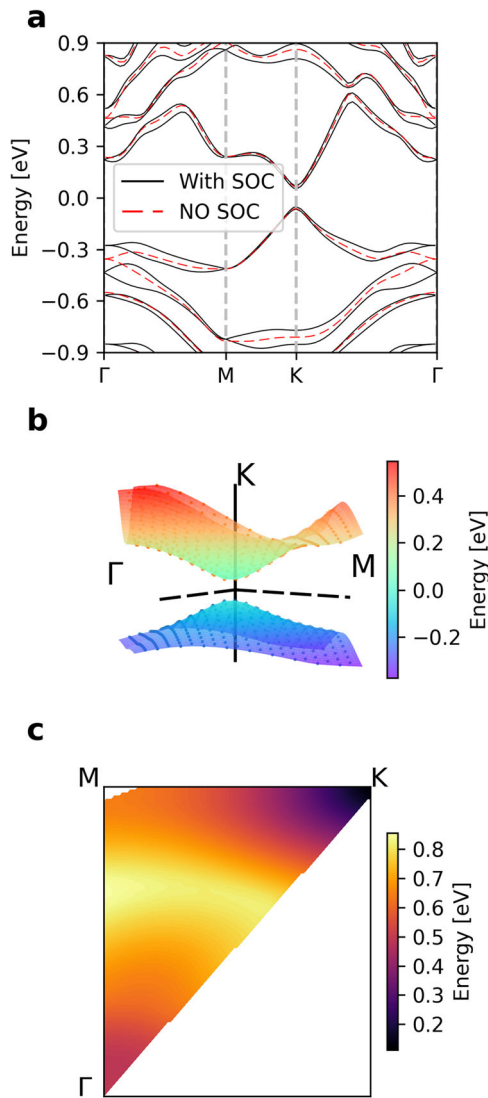
Fig. 2 Electronic band structure and heathmap. a Free-standing GeSn bilayer with (black) and without (red) SOI. **b** 3D plot of the lowest unoccupied band (red) and of the highest occupied band (blue) calculated in proximity of the point K. **c** Heatmap of the electronic energy gap calculated in the IBZ.

The shift of the Dirac point of stanene with respect to that of germanene, described by the diagonal Hamiltonian term $H_M = \text{diag}(M, M, -M, -M)$ plays a crucial role here. Additionally, the Ge and a-Sn have symmetry inverted band structures. Therefore when stanene and germanene form a covalently bonded bilayer, where gaps arise, band inversion can appear and dominate the properties. For this reason the parameters d and m, associated with the formation of direct and inverted bandgaps, respectively, as well as parameter M describing the shift of the Dirac cones are important. The equations for the bottom four bands are

$$E_{e1} = m/2 + d/2 + M;$$
$$E_{e2} = -m/2 + \sqrt{q^2 + (d/2 + M)^2}$$
$$E_{h1} = -m/2 - \sqrt{q^2 + (d/2 - M)^2}$$
$$E_{h2} = m/2 - d/2 - M$$

$$(2)$$

The equations confirm the formation of bandgaps and band shift. The conditions for band inversion occur when $E_{e1} = E_{h1}$ and
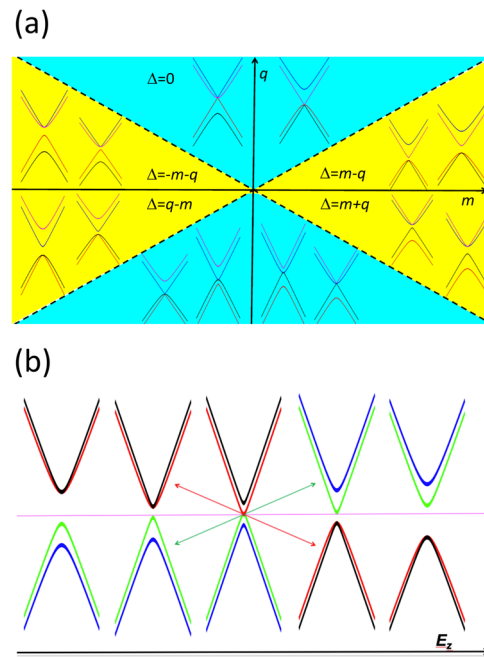
Fig. 3 Topological phase space and transition in the k · p-model. a Topology of the model described by the Hamiltonian, Eq. (8) as a function of parameters m and q. The zero gap ($\Delta = 0$) region is indicated in cyan, while the range of parameters giving a gapped band structure are marked in yellow. **b** An example of electronic band structure derived from the model Hamiltonian, Eq. (8) and from the eigenvalues of this Hamiltonian, presented by the Eqs. (1) for a small, constant value of q. The application of an electric field above a certain critical value can switch a hole band to an electron band (and vice versa).

$E_{e2} = E_{h2}$. The band inversion point is described by

$$m^2 - md + 2dM - 2mM = q^2 \qquad (3)$$

or

$$m^2 + md + 2dM + 2mM = q^2. \qquad (4)$$

Thus, the inversion point corresponds to the value $m = \pm q$ and $d = M = 0$ which agrees with the density functional theory (DFT) calculations, taking into account real parameter values for Ge and Sn. Here to make this comparison we have fitted the DFT numerical data for the shape of the bands in the vicinity of the K point by the d,m,q and M parameters of the developed the k · p-model. In principle, Eqs. (3), (4) indicate that band inversion can happen for a whole set of parameters, d,m,q and M. For band shifts the value of the parameter q, associated with the covalent bonding, is critical. Our analysis demonstrates that the covalent bonding between stanene and germanene in the bilayer is one possible origin for charge accumulation. The application of an external electric field polarizes the sublattices A and B of each monolayer and therefore strongly influences the parameters associated with the direct gap, d, and the shift of the Dirac cones, M. The electric field has no influence on the parameter m describing the inverted bandgap. The inverted bandgap is most strongly affected by parameter q which is the coupling between the stanene and germanene sublattices. Changing the value q displaces one of the stanene bands with respect to germanene decreasing the inverted bandgap. At a critical point of the topological phase transition the inverted bandgap vanishes and the inversion symmetry disappears, as proposed in 1985[12,47]. Details of the k · p-model analysis are summarized in the Supplementary Methods.

Bilayer synthesis

The proposed covalent GeSn bilayer structures were fabricated by alternatively depositing a germanene and a stanene layer on an appropriate substrate via electron beam deposition. The most successful substrate was sapphire (Al$_2$O$_3$), as suggested in[48,49]. Here, we have used a 60 nm Al$_2$O$_3$ substrate grown on Si wafer. The produced Ge monolayer was stable but allowed limited flexibility in the Ge atomic positions. Following the subsequent deposition of the Sn monolayer on top of the Ge a new slightly strained GeSn compound emerged. Crystallinity and homogeneity of the samples were confirmed by Raman spectroscopy. The thickness of the GeSn bilayer was estimated experimentally using the film deposition rate and time (see "Experiment"). The detailed analysis of SEM images indicates that the 0.3/0.3 nm GeSn bilayer is present as a uniform, homogeneous layer over the Al$_2$O$_3$ substrate on Si wafer (see Fig. 1c).

Optical properties

The optical properties of the GeSn bilayer were calculated within the independent particle approach starting from Eq. (6), with eigenvalues and eigenstates calculated at the DFT level.

The real part of the dielectric function of the GeSn bilayer, ε_1, has a value close to ~0 for energies around 15 eV, see Fig. 4a. This threshold energy is probably related to the plasma frequency in the bilayer, where the imaginary part ε_2 is close to zero. In the near ultra-violet and visible optical ranges ε_1 has negative values, reminiscent of a good metal, and rises very rapidly for energies below 2eV. The latter indicates that it is a highly polarizable quasi-two-dimensional system. Below 5 eV the imaginary part of the dielectric constant, $\varepsilon_2(\omega) = 4\pi \mathrm{Re}\, \sigma(\omega)/\omega$, which is proportional to an associated optical conductivity $\mathrm{Re}\, \sigma(\omega)$ demonstrates several maxima consisting of a series of peaks. Each peak in ε_2 is related to a rise in the density of states of a corresponding electron band. The lowest energy peak located near 0 eV is linked to transitions between Dirac like bands with a small gap. Such optical
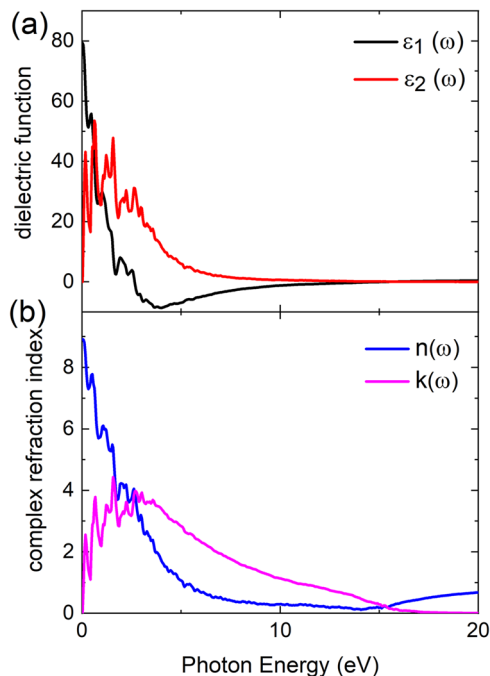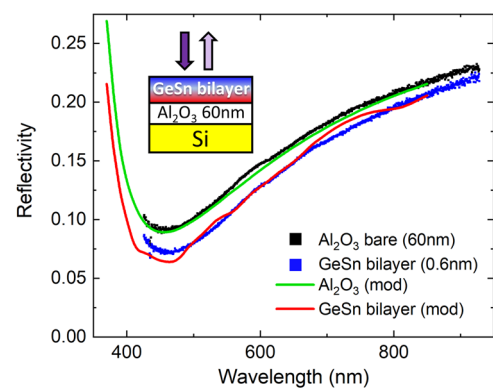
dependencies indicates that the GeSn bilayer is highly susceptible to incident light, due to the coupling of electrons from the Dirac like band.

The complex refraction index of the GeSn bilayer can be obtained from the complex dielectric function via simple relations $\varepsilon_1(\omega) = n(\omega)^2 - k(\omega)^2$ and $\varepsilon_2(\omega) = 2n(\omega)k(\omega)$. By solving these equations, $n(\omega)$ and $k(\omega)$ can be extracted, as shown in Fig. 4b. Notably, the refractive index $n(\omega)$ of the GeSn bilayer is less than ~1 for frequencies above 5 eV, where it is much smaller compared to the refractive indices of the Al$_2$O$_3$ substrate and the Si wafer, confirming its semi-metallic behaviour.

The existence of a semi-metallic layer on the surface of multilayer structures can significantly change the optical response, as was shown recently[50]. Specifically, zero reflectivity can be obtained by tuning the thickness of the metallic nanofilms in quadruple layer structures Si/Al$_2$O$_3$/Ge/Sn—exceeding state-of-the-art antireflective performance by an order of magnitude. The phenomenon was attributed to a reduction of the refractive index due to hybridization between the semi-metallic surface nanofilm and the underlying oxide.

To test the theoretical predictions, the optical reflectivity of the fabricated GeSn bilayer samples was measured by the ellipsometry technique. Notably, the presence of the GeSn bilayer overall reduces the reflectivity across all studied wavelengths reaching 20–25% around the minimum (see Fig. 5).

The experimental results are compared with the theoretically calculated reflectivities, that were obtained using the standard Fresnels equations and the transfer matrix method[50]. For the modelling, the complex refractive index of GeSn bilayer (see Fig. 4) has been determined theoretically from the ab-initio electronic structure calculations as described in the section "Ab-initio calculations". The other model input parameters—the refractive indices for—the Al$_2$O$_3$ and Si were obtained experimentally by the separate ellipsometry measurements of Si thick substrate with and without the Al$_2$O$_3$ thin film deposited in the house on the top. The agreement between theory and experiment is excellent (see, Fig. 5), showing that the material is highly susceptible to light and can be used to enhance impedance matching between the air and the substrate. The differences could be due to slight local misalignment between the individual monolayers during the deposition process. This would lead to the formation of strained flakes with different twist angles between the Ge and Sn monolayers alongside the stable bilayer configuration. The misaligned flakes would have a large unit cell and lattice strain breaking all

Fig. 4 Ab-initio optical response of the GeSN bilayer for in-plane light polarization. a Real and imaginary parts of the dielectric function for the GeSn-bilayer, $\varepsilon_1(\omega)$(in black) and $\varepsilon_2(\omega)$ (in red). b Real and imaginary parts of the refractive index for the GeSn-bilayer, $n(\omega)$ (in blue) and $k(\omega)$ (in pink).

Fig. 5 Experimental and computed optical reflectivity. Ellipsometry measurements of the optical reflectivity (dots) in the wavelength range of 400–950nm for the 60 nm thick Al$_2$O$_3$ substrate deposited on Si bulk (black) and the GeSn bilayer grown on top of the substrate (blue). The modelled reflectivity, obtained using a combination of ab-initio and transfer matrix methods (solid lines), is shown in green and red for the bare substrate and the GeSn bilayer, respectively.
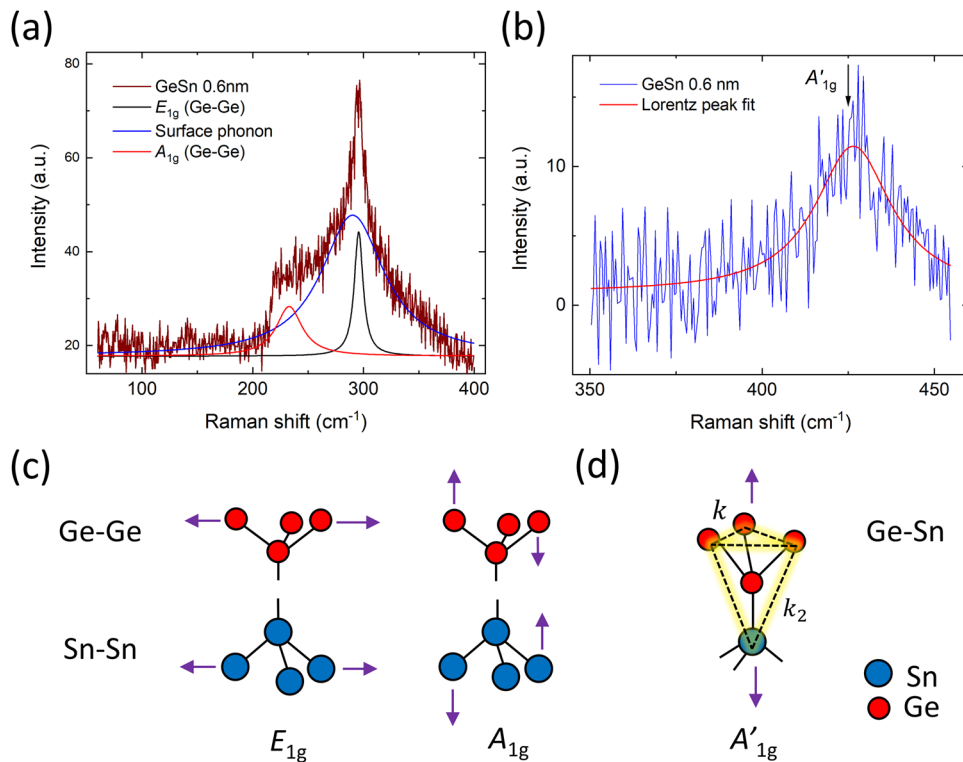
Fig. 6 Raman spectroscopy results for the GeSn bilayer. a The individual thickness of the Ge and Sn layers is estimated at ~0.3 nm. The Ge–Ge E_{1g} and A_{1g} modes are marked in black and red, respectively. The broad blue peak is attributed to surface phonons. **b** The A'_{1g} in GeSn bilayer can be well fitted with a Lorentzian form (in red), showing that the peak is well defined and has a narrow FWHM ≈ 25 cm^{-1}. **c** A schematic representation of the E_{1g} and A_{1g} vibrational modes in the Ge–Ge and Sn-Sn layers. **d** The transverse Ge–Sn A'_{1g} vibration. The local Ge–Sn pyramidal cluster is shown in yellow. k is the Ge–Ge spring constant and k_2 is the spring constant for the Ge–Sn bond. Ge and Sn atoms are shown in blue and red, respectively.

symmetries expect for spatial inversion. To illustrate this, we give a possible example of two monolayers of Ge and Sn twisted by 2.2° in the section "Ge/Sn bilayer with 2.2° twist".

Raman spectroscopy
The Raman spectroscopy results for the GeSn system are summarized in Fig. 6 and Supplementary Figs. 8, 9. Fig. 6a illustrates that only the Ge–Ge vibrational modes are visible in the GeSn bilayer below 400 cm^{-1}. The longitudinal vibrational mode E_{1g} is located at 295 ± 3 cm^{-1} and the transverse mode A_{1g} is found at 233 ± 3 cm^{-1}[51]. (The schematic representation of the vibrations is shown in Fig. 6c). Both Ge–Ge modes are well defined by a Lorentzian shape and have a narrow width (FWHM $\approx 15-20$ cm^{-1}), indicating good crystallinity. The location of the Ge–Ge modes is shifted to lower frequencies compared to those found in the Ge bulk material (~300 cm^{-1}) due to the proximity and strain coming from the Sn layer[52,53]. The Sn vibrations are absent due to the damping triggered by the large mass difference between the Ge and Sn atoms[53].

Furthermore, Fig. 6b shows a weak Raman mode at approximately 426 ± 3 cm^{-1} visible only in the GeSn bilayer. This mode disappears when the thickness of the individual Ge and Sn layers exceeds 0.5 nm, becoming too broad and weak in thicker films (see Supplementary Information). It is possible that the observed high-frequency mode is due to a transverse Ge–Sn bond vibration A'_{1g} (see, Fig. 6d).

To check this hypothesis, we introduce a localized Ge–Sn cluster treatment to estimate the transverse vibrational modes in the GeSn bilayer. In this approach a pyramidal Ge–Sn quasi-cluster is considered—where one central Ge atom is strongly coupled to three Ge atoms forming the base of the pyramid and one Sn atom

forming its apex (shown in Fig. 6d in yellow). The Ge–Sn quasi-clusters form due to strong, local lattice distortion in the Ge and Sn monolayers, where the central Ge atom acquires more pronounced sp^3 character. Using this representation, the frequency of the transverse vibration $\omega_{\text{Ge–Sn}} =$ of the central Ge atom inside the pyramidal Ge–Sn quasi-clusters is given by

$$\omega^2_{\text{Ge–Sn}} = \frac{1}{2}\left(\sqrt{(4a+b+g)^2 + 4(ab+4ag)} + 4a+b+g\right) \quad (5)$$

where the parameters a, b and g are elastic constants defined in terms of the interactions between the atoms and their masses. Therefore a is $a = \frac{k}{m}$ where k is the elastic constant of interaction between the Ge atoms and m is the Ge mass. Parameter b is $b = \frac{k_2}{m}$ with k_2 being the elastic constant of interaction between the Ge and the Sn atoms and m the mass of Ge.

Finally parameter g is $g = \frac{k_2}{m_2}$, where k_2 the interaction between Sn atoms and m_2 is Sn mass. In pure Ge the transverse Raman phonon mode has a simple qualitative frequency dependence $\omega_{\text{Ge}} = \sqrt{2k/m} = \sqrt{2a}$ where k is the elastic constant between Ge atoms, and $m/2$ is the reduced mass of two Ge atoms. From the literature, the frequency of the transverse Ge–Ge A_{1g} phonon mode is 300 cm^{-1}. Analogously the phonon frequency for the transverse Sn A_{1g} mode given by $\omega_{\text{Sn}} = \sqrt{2k_2/m_2} = \sqrt{2g}$ is ~160 cm^{-1}[53]. The masses of the Ge and Sn are 72.6 and 118.7 atomic units, respectively. Thus, the relation between parameters b and g is $b = g*118.7/72.63$. Substituting the estimated values for a, b and g into Eq. (5), the frequency of the transverse Ge–Sn mode in the bilayer is calculated as $\omega_{\text{Ge–Sn}} = 444$ cm^{-1}. The cluster-based estimate is extremely close to the experimentally observed high-frequency mode of 426 ± 3 cm^{-1}, supporting our hypothesis that it is indeed due to the transverse A'_{1g} vibration of the Ge atoms in the GeSn bilayer and could be taken as direct evidence thereof. In

summary, Raman spectra confirm the occurrence of the covalent GeSn bilayer and illustrate behaviours different from those found in Ge–Sn alloys[51,52].

Impedance spectroscopy in the GeSn bilayer

Complex impedance studies are widely used to determine the capacitance effects of grains and grain boundaries in polycrystalline materials[54–56]. It is a technique that can separate the behaviour of the material bulk from the grain boundary. More recently, such methods have become more widespread across the 2D community where they have been applied to probe for interfacial effect in ultra-thin films[57]. Thus, we apply complex impedance spectroscopy to study the behaviour on the interface between the GeSn bilayer and the Al_2O_3 oxide, which can be treated as a granular boundary. We compare two samples of GeSn bilayer grown together with Al_2O_3 oxide by different methods: e-beam deposition (e-beam) and atomic layer deposition (ALD). The ALD technique is expected to produce less surface roughness and result in more a single crystalline GeSn bilayer. Complex impedance for both GeSn samples was measured in the frequency range $0 < f < 100$ Hz or $0 < \omega < 600$ rad, see Fig. 7a. The real Z' and the imaginary Z'' parts of the complex impedance are shown as circles and triangles, respectively. Open symbols are used for GeSn bilayer grown by e-beam deposition, while closed symbols are used for those grown by the ALD technique. Notably, the ALD grown GeSn bilayer has slightly larger values of Z' and Z'' compared to the one produced by the e-beam method. Alternatively, the data can be represented as a Nyquist plot Z'' versus Z', as shown in Fig. 7b. The Nyquist plot has a characteristic semi-circular shape as reported in published literature[55,56], with ALD grown GeSn bilayer forming a slightly larger semicircle compared to the one produced by e-beam deposition (see, Fig. 7b open (closed) squares).

The experimental results for Z'' and Z' can be fitted by a parallel circuit RC model, described by Eq. (9). For the GeSn bilayer grown by e-beam deposition the best model fit to the experimental data is given by parameters $R = 65\ \Omega$ and $C = 1 \times 10^{-4}$ F (see, Fig. 7b red open stars). The low resistance value R may be attributed to surface effects, which dominate the properties at ultra-low material thicknesses, as was demonstrated for ultra-thin Bi multilayers[58]. Notably, the value of the capacitance is extremely large $C = 1 \times 10^{-4}$ F. We can approximate the capacitance by a simple parallel plate capacitor, with an area $A \sim 1 \times 10^{-5}$ m^2, a thickness d and a dielectric constant ε_0, (see Fig. 7c). The value for the dielectric constant of the GeSn bilayer $\varepsilon_0 \sim 70$ is calculated by DFT methods (see, Fig. 4a). Using these values we determine that the thickness of the capacitor is approximately $d \sim 0.1$ nm, roughly $\sim 1/6$ of the GeSn bilayer thickness. This confirms our premise that the capacitance effects are constrained to a narrow region around the GeSn bilayer and oxide interface. The capacitance between GeSn bilayer and the Al_2O_3 oxide may originate due to strain deformations at the interface that create local varying charge accumulation and distribution (see, Fig. 7c) as discussed in detail in the section "Possible origin of transverse electric field in GeSn bilayer".

Furthermore, using the obtained capacitance value C we may infer the average charge density q at the GeSn–oxide interface. The RMS AC current passing through the sample is $I_{RMS} = 2.8$ nA, giving an RMS voltage of $V_{RMS} = I_{RMS}*R$, where R is the RC model fit parameter $R = 65\ \Omega$. Thus, the RMS voltage across the GeSn bilayer is $V_{RMS-e-beam} = 1.8 \times 10^{-7}$ V. The charge of a capacitor is given by $Q = C*V_{RMS}$. Consequently, the charge stored in the GeSn bilayer capacitor is $Q_{e-beam} = 1.8 \times 10^{-11}$ C. Combining the stored charge with the area of the capacitor A, gives the average charge density $q = Q/A$, with $q_{e-beam} = 1.8 \times 10^{-6}$ C m^{-2}, which is approximately equal to an electron density of $n_{e-beam} \sim 1.1 \times 10^9$ cm^{-2}.
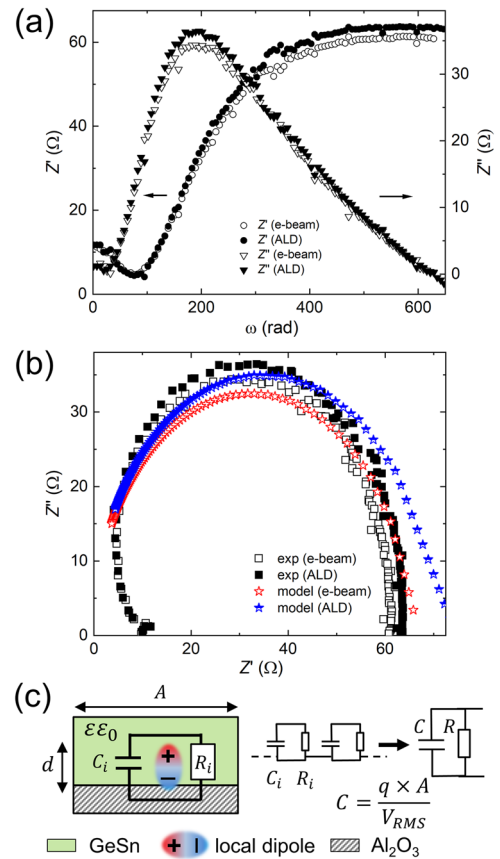
Fig. 7 Impedance measurements of the GeSn bilayer. Complex impedance of the GeSn bilayer in the frequency range $f = 1-100$ Hz. Open symbols refer to GeSn bilayer grown by e-beam method, while closed symbols denote those produced by ALD. **a** Real and imaginary parts of the complex impedance Z' (circles) and Z'' (triangles) as a function of frequency $\omega = 2\pi f$. **b** Nyquist plot: experimental values of Z'' plotted against Z' (squares); Z'' and Z' determined from the RC model (stars). **c** Schematic representation for the local dipole and charge density q formation at the GeSn bilayer to Al_2O_3 interface. The sum contribution of the local dipoles may be modelled as a parallel RC circuit.

For the GeSn bilayer grown by the ALD method best RC model parameters are $R = 70\ \Omega$ and $C = 8 \times 10^{-5}$ F, which is slightly higher (lower) compared to the e-beam deposition bilayer. The model fit to experimental data is reasonably good (see, Fig. 7b blue solid stars). Working through the parallel plate capacitor calculation, and assuming the same capacitor area A, we obtain the average charge density of $q_{ALD} = 1.6 \times 10^{-6}$ C m^{-2}. The average charge density q is thus approximately equal to electron density of $n_{ALD} \sim 1 \times 10^9$ cm^{-2}, which is $\sim 10\%$ lower than for the e-beam deposition grown GeSn bilayer. The discrepancy may be explained by the transverse interface surface roughness that is greater for samples grown by e-beam deposition technique compared to the ALD method. A greater surface roughness may lead to stronger buckling strain at the bilayer-oxide interface which will result in larger capacitance C and charger density q, as has been observed experimentally. Notably, here the charge density q is dipole-like, see Fig. 7c which may indicate the presence of ferroelectricity in this material.

The origin of ferroelectricity is related to the breaking of spatial inversion symmetry P. Here, we have found that the formation of the GeSn bilayer gives rise to a redistribution of electric charge between the Ge and Sn monolayers generating an intrinsic electric field between the layers. The system is reminiscent of a charged parallel plate capacitor. Such inversion symmetry breaking process

is also accompanied by strong lattice distortion for some of the Ge and Sn atoms, creating effective electric dipoles. Electric dipole presence is confirmed theoretically by our ab-initio simulations (see Supplementary Fig. 7 and Supplementary Fig. 5) and $k \cdot p$-model analysis as well as experimentally from impedance spectroscopy results (see Fig. 7c). All dipoles are electrically ordered perpendicular to the Ge and Sn monolayer planes therewith forming a ferroelectric state. Our results reveal remarkable agreement between ab-initio calculations and impedance spectroscopy measurements (see Fig. 7c and Supplementary Fig. 5). Thus, the combination of ab-initio simulations and $k \cdot p$-model analysis and the comparison with the impedance spectroscopy experiments indicates that the GeSn bilayer is intrinsically a ferroelectric material where the internal electric field is oriented perpendicular to the 2D layers.

Possible origin of transverse electric field in GeSn bilayer

Introducing an internal electric field into the GeSn bilayer is highly desirable because it may allow exploration of the topological phase transformations predicted by the $k \cdot p$ method. However, we have demonstrated theoretically using DFT methods that an externally applied electric field is not a suitable tuning parameter as it induces a trivial insulator-to-metal transition before the topological character can manifest in the GeSn bilayer. Prior to that transition the application of an external electric field of $E = 0.01$ a.u. induces a dipole-like charge density accumulation between stanene and germanene layers of the order of $q_{th} = 0.15$ μe $Å^{-2}$, where the stanene becomes more positively and the germanene negatively charged, as shown in Supplementary Fig. 5b).

The dipole-like charge density as obtained from the analysis of our impedance studies by the RC and parallel plate capacitor models is $q_{e-beam} = 1.8 \times 10^{-6}$ C m^{-2} and $q_{ALD} = 1.6 \times 10^{-22}$ C m^{-22}, for the two methods of bilayer growth, respectively. We can convert it to $q_{e-beam} = 0.11$ μe $Å^{-2}$ and $q_{ALD} = 0.10$ μe $Å^{-2}$, which are remarkably similar to q_{th}. By comparing these values, we may estimate the transverse electric fields consistent with the formation of such dipole charge densities as $E_{trs-e-beam} \sim 0.0073$ a.u. and $E_{trs-ALD} \sim 0.0067$ a.u. for the two respective samples. This effect may be enhanced and controlled by suitably doping the substrate with p or n type impurities.

Overall, by choosing a substrate we may control the local transverse buckling strain in the bilayer to induce an effective electric field in between the Ge and Sn monolayers. The electric field arises due to charge accumulation in the space between stanene and germanene that will manifest as a local peak in the potential superposed on top of the covalent bonding. This phenomenon has been shown to occur theoretically through a rigorous comparison of charge density analysis and covalent bonding where local strain produces local electron accumulation and an associated peak in electric potential ref. [59]. An electric field of this nature may be numerically modelled as a saw-tooth potential as demonstrated in several literature examples[60]. Therefore, we suggest, that the choice of substrate will produce a local effective electric field perpendicular to the GeSn bilayer. Additionally, the electric field may influence the covalent bond length in the GeSn bilayer, providing a viable tuning mechanism for the investigation of its topological properties. As the electric field is local on the nanoscale, we may avoid the bulk metal-to-insulator transition predicted by the DFT calculations. We may thus speculate that an appropriate choice of substrate would allow us to engineer and control the perpendicular strain and consequently the topological GeSn bilayer properties.

Numerous examples in the literature indicate that substrates on which the bilayers are grown may significantly alter the properties. Specifically the phenomenon of charge redistribution has been frequently observed in many two-dimensional materials[61–66]. In particular, in graphene grown on SiC substrate there arises a charge redistribution[62,63] producing a minigap in its energy spectrum and influencing strongly its photoresponses[64]. The analogous spontaneous charge redistribution between graphene and P3HT improves significantly the conversion efficiency in graphene based organic solar cells[67,68]. In the illustrative case of FeSe, the choice of substrate converts the material to either a superconductor with a T_c above 65 K (grown on SrTiO$_3$) or an insulator[69–71]. In FeSe charge accumulation, similar to the scenario proposed here, plays a key role.

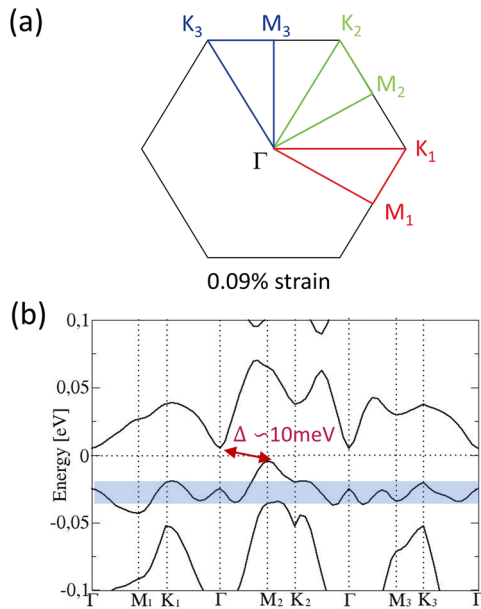### Ge/Sn bilayer with 2.2° twist

For comparison, we have performed a calculation of a GeSn bilayer structure with a twist angle of 2.2°. Our discovery showed that covalent bonding can exist between germanene and stanene in such twisted structure. The strong covalent bonding between the Ge and Sn atoms significantly changes the local geometry of the atomic bonds leading to a very large new unitary cell containing 182 atoms. Notably, the lattice strain in this structure is 0.09%, the same as for 30° twisted GeSn cell. However, in this new geometry such lattice strain is much more significant, due to the unit cell being very large and giving rise to extremely narrow energy bands. Thus, relatively small lattice distortions triggered by the 0.09% strain can modify the bands substantially. Contrary to the 30° twisted bilayer, the 2.2° twisted lattice is more disordered, as the Ge and Sn atoms undergo numerous minute displacements to minimize the total energy. As a result the system looks almost completely disordered (see, Fig. 8 and Supplementary Figs. 1, 2). However, the thickness of the 2.2° twisted bilayer remains unchanged around 6 Å (see, Fig. 8b), as in the 30° twisted bilayer case (see, Fig. 1b).

Ideally, in the case of 2.2° twisted bilayer the crystal structure should assume a C_3 or more precisely, D_{3d}, symmetry point group, similar to the 30° twisted GeSn bilayer (Fig. 1c). The 2.2° twisted GeSn bilayer has an O(2) symmetry and a hexagonal BZ with the points K_1, K_2, K_3 and M_1, M_2 and M_3, corresponding to the unit cell with 182 atoms (see, Fig. 9a). Without lattice distortions all K and M points have degenerate bandgaps. The six-fold O(2) degeneracy is related to the breaking of the original C_3 symmetry in the unrelaxed unit cell. However, due to the extensive distribution of
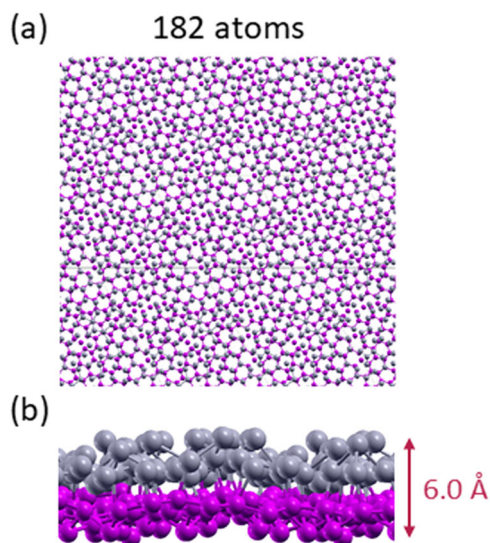
Fig. 8 Equilibrium geometry of the 2.2° twist-angle GeSn bilayer. a Top view of the unitary cell containing 182 atoms. The lattice strain is 0.09%. All atoms experience lattice distortions both in the xy-plane and in the z direction. **b** Side view showing significant lattice distortions in the vertical z direction. The thickness of this type of bilayer is around 6 Å, same as for the 30° twist-angle cell.

Fig. 9 Brillouin zone and band structure of the 2.2° twisted bilayer. a The hexagonal BZ for the 2.2° twisted GeSn bilayer; the points K_1, K_2, K_3 and points M_1, M_2 and M_3 correspond to the unit cell consisting of 182 atoms. Without lattice distortions all K and M points have degenerate bandgaps. The degeneracy is broken when lattice distortions break lattice symmetry to minimize the total energy. **b** Electronic band structure of the 2.2° twisted GeSn bilayer, where the centre of inversion is absent, demonstrating flat bands and an indirect bandgap of 10 meV.

strain around the unit cell, triggered to minimize the interatomic forces, there is a breaking of the D_{3d} symmetry for both the individual germanene and stanene layers. As a result, the degeneracy is broken and all K and M points will have a different value of the energy gap. The electronic band structure for the 2.2° twisted GeSn bilayer is shown in Fig. 9b, demonstrating inversion in k space due to the existence of time-reversal symmetry. The electronic gap Δ is indirect, of about $\Delta \approx 10$ meV. The hole band becomes very narrow and flat (shown in blue shading). The breaking of inversion symmetry, P and lattice symmetry D_{3d} may happen along three different directions. Thus, the effective displacement of atoms breaking the inversion symmetry P in the new unit cell may occur along one of three orientations as dictated by the C_3 rotational elements.

These C_3 symmetry breaking atomic displacements are, probably, associated with a relative shift of the Ge and Sn atoms, where the centre of inversion vanishes, leading to the creation of an internal in-plane electric field. This internal electric field may be different across different unit cells. Notably, the Mermin–Wagner–Hohenberg (MWH) Theorem states that no phase with spontaneous breaking of a continuous symmetry can exist for $T > 0$, in $d \leq 2$ dimensions[39,72]. Thus, according to MWH the 2.2° twisted GeSn bilayer is unstable and will be decomposed into numerous domains, with a different orientation of the in-plane electric fields. As a result, there may be a large variety of in-plane electric field configurations within the 2.2° twisted GeSn bilayer. The electric field may be locally ordered or disordered, which is dictated by the respective atomic position displacements. This complex proposed scenario is reminiscent of the $p - n$-junctions in graphene where the magnetic field induces boundary edge currents and snake states[73], leading to a rich physics of topological defects. Analogous, covalent bilayers such as GeSn may realize completely unexplored physics of strain-tuned ferroelectric domains.

DISCUSSION

We have shown that the interaction between two monolayers of germanene and stanene creates a covalent GeSn bilayer. This 2D material exhibits a complex unit cell and emergent properties and symmetries providing linear bands, reminiscent of the Dirac cones. Our DFT calculations reveal that this covalent GeSn bilayer can exhibit an insulator-metal transition in an applied external electric field, a property useful in the fabrication of fast 2D electronic transistors. In addition, with the support of the $\mathbf{k} \cdot \mathbf{p}$ model we show that a quantum phase transition from trivial to topological insulator can occur. Using impedance spectroscopy studies we demonstrate that the GeSn bilayer may also be highly susceptible to the choice of substrate. The strain at the bilayer/substrate interface leads to transverse buckling deformations and charge accumulation between the Ge and Sn monolayers. The effect manifests as a local dipole-like charge density q which can be expressed as a local transverse electric field E_{trs}. We suggest that by controlling the local transverse electric fields in the GeSn bilayer through substrate-induced strain imposed, for example, by a choice of substrate, we may probe the topological characteristics and transformations as predicted by the $\mathbf{k} \cdot \mathbf{p}$ model.

Moreover, we have discovered a covalent GeSn bilayer structure —where the twist angle between the monolayers is 2.2°. This slightly disordered bilayer is an indirect semiconductor with nearly flat bands and a narrow indirect gap of approximately ~10 meV. We expect that this system will have unconventional superconductivity due to its topologically flat band structure, as described in ref. [74], strong correlations associated with the flatness of the band, and other effects similar to those found in bilayer graphene[16–22]. The bandgap in 2.2° twisted GeSn bilayer is narrow enough to be excited at the terahertz frequency, making it an option for new sources of terahertz waves.

We have confirmed the existence of the GeSn bilayer experimentally through ellipsometry reflectivity, Raman and impedance spectroscopies. The reflectivity results are fitted extremely well by a model that assumes the presence of the GeSn bilayer. Raman spectroscopy demonstrates a high-frequency mode at 426 ± 3 cm^{-1} that is consistent with the vibration of the transverse Ge–Sn covalent bond in the bilayer. The impedance spectroscopy shows the existence of a high capacitance $C = 1 \times 10^{-4}$ and dipole-like charge density $q = 1.8 \times 10^{-6}$ C m^{-2} or $q = 0.11$ μe Å^{-2} confined to a narrow region (~1/6 of the bilayer thickness) at the bilayer-oxide interface. The effect may be linked substrate-induced transverse strain and buckling of the bilayer, and has randomly local character. Notably, the capacitance is highly sensitive to the growth method and surface roughness of the oxide and bilayer. For oxide and GeSn bilayer grown by the ALD method, which produces less surface roughness (and less perpendicular strain and buckling) the capacitance and the associated charge density is lower by ~ 10%. Consequently, the capacitance (charge accumulation) effect may be enhanced (or reduced) by an appropriate choice of substrate (and its growth method). Exploring and utilizing the proposed substrate-controlled charge accumulation in the GeSn bilayer may have significant potential for realizing 2D ferroelectric materials with topological characteristics.

Furthermore, the substrate-strain-induced dipole-like charge density q, by comparisons with DFT calculations, may be converted to an electric field E_{trs}. We estimate that the transverse electric field for the GeSn bilayer grown by e-beam deposition is $E_{trs} \sim 0.0073$ a.u. and slightly lower ($E_{trs} \sim 0.0067$ a.u.) for ALD-grown bilayer. This electric field has a local and random character which is unlikely to trigger the insulator-to-metal transition that has been predicted to occur in GeSn bilayer in a static external electric field. Thus, the strain-induced electric field may provide a reliable method for tuning and controlling its topological properties. The ability to switch topologically protected states on and off

by strain-induced local electric fields would allow harnessing the properties of massless Dirac electrons in a new era of optoelectronic devices. Coupled with the GeSn bilayer high sensitivity to light, this discovery may have significant implications for the development of novel 2D material for sustainable solar energy and energy storage technologies.

The proposed simplicity in the fabrication of the covalent bilayers and their versatility may open up new directions in the development and design of quantum technologies. Covalent bilayers are much more stable and robust to surface impurities and lattice imperfections, which coupled with their potential for topologically protected states, would make them ideal building blocks for qubits, quantum gates and novel van der Waals materials. Therefore, the class of 2D materials—based on covalently bonded bilayers reported here, may facilitate a broad range of technological advances and discoveries.

METHODS

Ab-initio calculations

Ab-initio calculations were performed within the DFT plane-wave Quantum Espresso (QE) code[75] employing the Perdew-Burke-Ernzerhof generalized gradient approximation[76]. We have used full-relativistic ultrasoft pseudopotentials in order to include SOI within the scheme described in[77,78]. Periodic images of the GeSn bilayer were positioned far enough to avoid interaction. A Γ centred $6 \times 6 \times 1$ **k**-points grid was used for the determination of the equilibrium structure.

An energy cutoff of 80 Ry and one of 420 Ry were used, respectively, for the wave functions and for the charge density. When required, an electric field has been applied to the material, by adding a saw-tooth potential such that the field is constant across the entire sample, and the magnitude of the field is dictated by the slope of the saw-tooth.

Optical properties were calculated within the independent particle approach using the Fermi golden rule:

$$\text{Im}[\varepsilon_{ii}^{SL}(\omega)] = \frac{8\pi^2 e^2}{m^2\omega^2 V} \sum_{\mathbf{k}} \sum_{v,c} |p_{vc,k}^i|^2 \delta(E_c(\mathbf{k}) - E_v(\mathbf{k}) - \hbar\omega) \quad (6)$$

where $\varepsilon_{ii}^{SL}(\omega)$ is the dielectric function of the supercell, V is its volume, $p_{vc,k}^i$ is the momentum matrix element, and $E_i(\mathbf{k})$ the eigenvalue of band n at $\mathbf{k}$. The indexes v, c stand for valence and conduction band, respectively, whereas $i = x, y, z$ describes the light polarization. In order to extract the dielectric function of the bilayer ε_{ii}^{GeSn}, we use the relation (valid for light polarized in the xy-plane defined by the bilayer):

$$L\varepsilon_{ii}^{SL}(\omega) = D + d\varepsilon_{ii}^{GeSn}(\omega) \quad (7)$$

with $L = D + d$ the length, along z, of the supercell box, D the vacuum region and d the thickness of the GeSn bilayer. Estimating $d \sim 6$ Å, we determine $\varepsilon_{ii}^{GeSn}(\omega)$. From there, the refractive index n and the extinction coefficient k follow. A mesh of $72 \times 72 \times 1$ **k**-points grid was used for the calculation of the optical properties. The real part of the dielectric function, ε_1, is then obtained using conventional Kramers-Kronig relations.

The topology of the system is characterized by a $\mathbb{Z}_2$ index (v)[34]. If v is even, $(v = 0)$ the system is a trivial insulator adiabatically connected to an atomic insulator or to the vacuum. If v is odd $(v = 1)$ it is a topological quantum spin Hall insulator[33,79], where the quantum spin Hall effect can manifest through a spin pumping process[33,79]. The $\mathbb{Z}_2$ invariant is computed using the Z2pack package[80], by tracking the evolution of the 1D hybrid Wannier charge centres as described in ref.[81]. Further computational details are reported in the Supplementary Methods.

k · p-model

In order to understand what phenomena may exist in GeSn bilayer we introduced an effective **k** · **p** simplified 4x4 Hamiltonian. Here we are considering only one valley, e.g. the one at K, and neglecting for simplicity the spin degrees of freedom, based on only the symmetry arguments. Therewith we may obtain the following simplified Hamiltonian for the bilayer (see the derivation in the Supplementary Methods):

$$H = \begin{pmatrix} \frac{(m+d)}{2} & k_x - ik_y & 0 & 0 \\ k_x + ik_y & -\frac{(m+d)}{2} & q & 0 \\ 0 & q & \frac{(d-m)}{2} & k_x - ik_y \\ 0 & 0 & k_x + ik_y & \frac{(m-d)}{2} \end{pmatrix} \quad (8)$$

where for convenience we have parametrized the germanene and stanene gaps, m_1 and m_2, respectively by two parameters, m and d. Here $m = m_1 - m_2$ and $d = m_1 + m_2$. Note, that such parametrisation is convenient since the parameter m is directly related to the symmetry breaking, which can be associated with the charge transfer between the Ge and Sn layers. Such charge transfer will create an internal electrical field originating between the layers and oriented perpendicular to the 2D planes. In addition to the above described parameters for the charge transfer gaps, m and d, we have also introduced a term related to the charge transfer interaction or a polarization arising between Ge and Sn monolayers q. This term corresponds to the interaction, or overlapping integral (hopping), between the B sub-lattice of Ge and the A sub-lattice of Sn or vice versa, depending on which of the sublattices of Sn and Ge are closest to each other. Here we also used the dimensional natural units, where also $v_F = 1$. Note that all these parameters, m, d and q, may depend linearly on applied transverse electric field (see the detail discussion in ref.[39]). A detailed derivation of Eq. (8) is given in the Supplementary Methods.

Experiment

All samples have been grown with e-beam deposition in the electron beam evaporator (HHV TF600) under clean room Class "100" conditions at a very high vacuum. The deposition rates varied. The substrates were chemically and ultrasonically cleaned by solutions of Decon 90 (5%), deionized (DI) water and ethanol sequentially for 5 and 15 min intervals. The substrates were dried softly under high-purity nitrogen gas and studied by SEM. The sapphire Al_2O_3 layer was grown on top of the cleaned pure n-doped Si substrates with a deposition rate of 1 Å per second. The GeSn bilayers were deposited on top of the Al_2O_3 thin film under high vacuum (10^{-7} mbar). Here the lowest deposition rate of 0.2 Å per second was applied to get highest quality bilayers. For experimentally studied GeSn samples, the thickness of the individual layers was determined using the film deposition rate and time. The sample surface morphology was investigated using high-resolution SEM (FEI Nova NanoSEM 450). The reflectivity (s and p polarization) was measured by ellipsometry with different incident angles (from 30° to 90°) over a broad range of wavelengths from 200 nm to 2500 nm. The effective refractive index (n) and extinction coefficient (k) have been measured directly by the same ellipsometry setup at 70° angle of incidence. The reflectivity results were modelled by considering a multilayer system composed of the GeSn bilayer, the Al_2O_3 substrate and the Si wafer, as seen in the cross-section SEM images in Fig. 1d. The multilayer system is considered as a single effective medium characterized by effective optical constants that depend on the optical properties of its constituents. The amplitudes of the electric and magnetic fields arising on the interface between the air, the GeSn bilayer, the Al_2O_3 substrate and the Si wafer are calculated using standard Fresnel equations and the transfer

matrix theory ref. [50]. The field amplitudes determine the effective complex refractive index of the multilayer system and hence can be used to obtain reflectivities Fig. 5. Raman spectroscopy was performed using Horiba Raman spectrometer with a green He-Ne laser of wavelength 532 nm. Diffraction grating of 600 gr/mm was sufficient to produce high resolution in the experiments. The laser power and acquisition time varied between 0 - 10% of nominal power 1mW and 1–10s, respectively, to prevent sample over-heating effects, peak and background broadening. The laser beam was focused to 1 μm spot-size on the surface of the samples. The Raman peaks were fitted using Lorentzian form to determine peak position and full width half maximum (FWHM). The Raman spectra are collected at multiple sample locations to confirm the uniform crystallinity of the films.

Complex impedance studies in the GeSn bilayer were performed using a setup consisting of a lock-in amplifier (Standford Research SR830) and a room temperature transformer. The lock-in amplifier was used to generate a sinusoidal output voltage $V_{sin}(f) \sim 0.004$ V. The sine wave reference signal was then passed across a fixed resistor $R \sim 1$ MΩ, converting it to an AC current of magnitude $I_{AC}(f) = 4$ nA with a particular frequency f. The GeSn bilayer was contacted with gold (Au) wire of 25 μm diameter in a standard linear 4-probe configuration. Silver paint was used to provide good electrical contact between the Au wire and the bilayer surface. The Au wires were reinforced externally with Araldaite rapid epoxy for mechanical stability. The AC current I_{AC} was passed across the outer two electrodes of the bilayer, and AC voltage V_AC was picked up across the inner two electrodes. The AC voltage signal V_{AC} was passed through a room temperature transformer with a gain $G \sim 100$ to enhance the signal-to-noise ratio and reduce noise. The lock-in amplifier collected both the in-phase and out-of-phase contributions of the V_{AC} signal—V_{AC}(in) and V_{AC}(out). Real and imaginary parts of the complex impedances were then calculated as $Z' = V_{AC}(\text{in}) / (100 \times I_{AC})$ and $Z'' = V_{AC}(\text{out})/(100 \times I_{AC})$, respectively. This method for studying complex impedances was tested previously in the literature and has been seen to agree with results from conventional impedance analyzers in the low frequency range up to ~ 300 Hz[82,83]. A particular advantage of the lock-in amplifier setup is that it is considered to be the least invasive technique, even suitable for biological specimens[82]. Using this preferred method for determining the complex impedance in the system ensured that the GeSn bilayer was not irreversibly or destructively affected in the course of these studies. The complex impedance results were simulated by a conventional RC-model, where a resistor R and a capacitor C are connected in parallel. In this manner, the real and imaginary parts of the complex impedance are given by

$$Z' = \frac{R}{1 + (\omega RC)^2}, \quad Z'' = \frac{\omega R^2 C}{1 + (\omega RC)^2} \qquad (9)$$

where R and C are the resistor and capacitor, respectively, and ω is the excitation frequency $\omega = 2\pi f$, as detailed in the literature[54].

DATA AVAILABILITY
The data that support the findings of this study are available from the corresponding author upon reasonable request.

CODE AVAILABILITY
All DFT calculations were performed with the QE open-source package, freely available at https://gitlab.com/QEF/q-e. The Z2 invariant calculations are performed with the Z2pack open-source package, freely available at https://z2pack.greschd.ch/en/latest.

REFERENCES
1. Geim, A. K. Graphene: status and prospects. *Science* **324**, 1530–1534 (2009).
2. Geim, A. K. & Novoselov, K. S. The rise of graphene. *Nat. Mater.* **6**, 183–191 (2007).
3. Li, L. et al. Black phosphorus field-effect transistors. *Nat. Nanotechnol.* **9**, 372 (2014).
4. Koenig, S. P., Doganov, R. A., Schmidt, H., Castro Neto, A. H. & Oezyilmaz, B. Electric field effect in ultrathin black phosphorus. *Appl. Phys. Lett.* **104**, 103106 (2014).
5. Liu, H. et al. Phosphorene: an unexplored 2d semiconductor with a high hole mobility. *ACS Nano* **8**, 4033–4041 (2014).
6. Vogt, P. et al. Silicene: compelling experimental evidence for graphenelike two-dimensional silicon. *Phys. Rev. Lett.* **108**, 155501 (2012).
7. Bechstedt, F., Matthes, L., Gori, P. & Pulci, O. In: Vogt, P. & Guy L. L. (eds). *Silicene: Prediction, Synthesis, Application* 73–98 (Springer, 2018).
8. Das, S., Robinson, J. A., Dubey, M., Terrones, H. & Terrones, M. Beyond graphene: progress in novel two-dimensional materials and van der Waals solids. *Annu. Rev. Mater. Sci.* **45**, 1–27 (2015).
9. Manzeli, S., Ovchinnikov, D., Pasquier, D., Yazyev, O. V. & Kis, A. 2D transition metal dichalcogenides. *Nat. Rev. Mater.* **2**, 1–15 (2017).
10. Bonaccorso, F., Sun, Z., Hasan, T. A. & Ferrari, A. C. Graphene photonics and optoelectronics. *Nat. Photon.* **4**, 611 (2010).
11. Tao, L. et al. Silicene field-effect transistors operating at room temperature. *Nat. Nanotechnol.* **10**, 227–231 (2015).
12. Kusmartsev, F.V. & Tsvelik, A.M. Semimetallic properties of a heterojunction. *JETP Lett.* **42**, 257–260 (1985).
13. Bechstedt, F., Gori, P. & Pulci, O. Beyond graphene: clean, hydrogenated and halogenated silicene, germanene, stanene, and plumbene. *Prog. Surf. Sci.* **96**, 100615 (2021).
14. Gong, Y. et al. Vertical and in-plane heterostructures from Ws$_2$/MoS$_2$ monolayers. *Nat. Mater.* **13**, 1135–1142 (2014).
15. Prete, M. S., Mosca Conte, A., Gori, P., Bechstedt, F. & Pulci, O. Tunable electronic properties of two-dimensional nitrides for light harvesting heterostructures. *Appl. Phys. Lett.* **110**, 012103 (2017).
16. Cao, Y. et al. Unconventional superconductivity in magic-angle graphene superlattices. *Nature* **556**, 43 (2018).
17. Cao, Y. et al. Correlated insulator behaviour at half-filling in magic-angle graphene superlattices. *Nature* **556**, 80 (2018).
18. Yankowitz, M. et al. Tuning superconductivity in twisted bilayer graphene. *Science* **363**, 1059–1064 (2019).
19. Shen, C. et al. Correlated states in twisted double bilayer graphene. *Nat. Phys.* **16**, 520–525 (2020).
20. Moriyama, S. et al. Observation of superconductivity in bilayer graphene/hexagonal boron nitride superlattices. Preprint at https://arxiv.org/abs/1901.09356 (2019)
21. Zheliuk, O. et al. Josephson coupled ising pairing induced in suspended MoS$_2$ bilayers by double-side ionic gating. *Nat. Nanotechnol.* **14**, 1123–1128 (2019).
22. Zhang, X. et al. Transition metal dichalcogenides bilayer single crystals by reverse-flow chemical vapor epitaxy. *Nat. Commun.* **10**, 598 (2019).
23. Arcudia, J., Emrem, B., Heine, T. & Merino, G. The structural and electronic richness of buckled honeycomb asp bilayers. *Nanoscale* **14**, 10136–10142 (2022).
24. Arcudia, J., Kempt, R., Eduardo Cifuentes-Quintal, M., Heine, T. & Merino, G. Blue phosphorene bilayer is a two-dimensional metal and an unambiguous classification scheme for buckled hexagonal bilayers. *Phys. Rev. Lett.* **125**, 196401 (2020).
25. Huang, C. et al. Quantum phase transition in germanene and stanene bilayer: from normal metal to topological insulator. *J. Phys. Chem. Lett.* **7**, 1919–1924 (2016).
26. Matthes, L., Pulci, O. & Bechstedt, F. Massive dirac quasiparticles in the optical absorbance of graphene, silicene, germanene, and tinene. *J. Condens. Matter Phys.* **25**, 395305 (2013).
27. Matthes, L., Pulci, O. & Bechstedt, F. Optical properties of two-dimensional honeycomb crystals graphene, silicene, germanene, and tinene from first principles. *New J. Phys.* **16**, 105007 (2014).
28. Zhu, F.-F. et al. Epitaxial growth of two-dimensional stanene. *Nat. Mater.* **14**, 1020–1025 (2015).
29. Hartman, T. & Sofer, Z. Beyond graphene: chemistry of group 14 graphene analogues: silicene, germanene, and stanene. *ACS nano* **13**, 8566–8576 (2019).
30. Qihang, K. N. et al. Tunable bandgap in silicene and germanene. *Sci. Rep.* **12**, 113–118 (2012).
31. Yang, J., Goh, K. E. J., Yu, Z. G., Wong, R. E. & Zhang, Y.-W. A first-principles study on strain engineering of monolayer stanene for enhanced catalysis of CO$_2$ reduction. *Chemosphere* **268**, 129317 (2021).
32. Thouless, D. J., Kohmoto, M., Nightingale, M. P. & den Nijs, M. D. Quantized Hall conductance in a two-dimensional periodic potential. *Phys. Rev. Lett.* **49**, 405 (1982).

33. Kane, C. L. & Mele, E. J. Quantum spin hall effect in graphene. *Phys. Rev. Lett.* **95**, 226801 (2005).

34. Kane, C. L. & Mele, E. J. Z₂ topological order and the quantum spin Hall effect. *Phys. Rev. Lett.* **95**, 146802 (2005).

35. Liu, C.-C., Jiang, H. & Yao, Y. Low-energy effective hamiltonian involving spin-orbit coupling in silicene and two-dimensional germanium and tin. *Phys. Rev. B* **84**, 195430 (2011).

36. Xu, Y. et al. Large-gap quantum spin hall insulators in tin films. *Phys. Rev. Lett.* **111**, 136804 (2013).

37. Zhang, G. & Zhang, Y.-W. Exploring ag(111) substrate for epitaxially growing monolayer stanene: a first-principles study. *Sci. Rep.* **6**, 2910 (2016).

38. Yuhara, J. et al. Large area planar stanene epitaxially grown on ag(1 1 1). *2D Mater.* **5**, 025002 (2018).

39. O'Hare, A., Kusmartsev, F. V. & Kugel, K. I. A stable "flat" form of two-dimensional crystals: could graphene, silicene, germanene be minigap semiconductors? *Nano Lett.* **12**, 1045–1052 (2012).

40. Grassano, D. et al. Detection of topological phase transitions through entropy measurements: the case of germanene. *Phys. Rev. B* **97**, 205442 (2018).

41. Houssa, M. et al. Topological to trivial insulating phase transition in stanene. *Nano Res.* **9**, 774–778 (2016).

42. Tang, P. et al. Stable two-dimensional dumbbell stanene: a quantum spin hall insulator. *Phys. Rev. B* **90**, 121408 (2014).

43. Ezawa, M. Monolayer topological insulators: Silicene, germanene, and stanene. *J. Phys. Soc. Japan* **84**, 121003 (2015).

44. Ma, Y., Kou, L., Du, A. & Heine, T. Group 14 element-basd non-centrosymmetric quantum spin hall insulators with large bulk gap. *Nano Res.* **8**, 3412–3420 (2015).

45. Koda, D. S., Friedhelm, B., Marques, M. & Teles, L. K. Coincidence lattices and interlayer twist in van der Waals heterostructures: application of the coincidence lattice method on hBN/MoSe₂hBN/MoSe₂ heterobilayer systems. *J. Electron. Mater.* **46**, 3910–3916 (2017).

46. Ezawa, M. A topological insulator and helical zero mode in silicene under an inhomogeneous electric field. *New J. Phys.* **14**, 033003 (2012).

47. Volkov, B. A. & Pankratov, O. A. Two-dimensional massless electrons in an inverted contact. *JETP* **42**, 178 (1985).

48. Grazianetti, C. et al. Optical conductivity of two-dimensional silicon: evidence of Dirac electrodynamics. *Nano Lett.* **18**, 7124–7132 (2018).

49. Gori, P., Kupchak, I., Bechstedt, F., Grassano, D. & Pulci, O. Honeycomb silicon on alumina: massless dirac fermions in silicene on substrate. *Phys. Rev. B* **100**, 245413 (2019).

50. Zhang, B., Liu, Y., Luo, Y., Kusmartsev, F. V. & Kusmartseva, A. Perfect impedance matching with meta-surfaces made of ultra-thin metal films: a phenomenological approach to the ideal THz sensors. *Mater.* **13**, 5417 (2020).

51. Arguilla, M. Q., Jiang, S., Chitara, B. & Goldberger, J. E. Synthesis and stability of two-dimensional Ge/Sn graphane alloys. *Chem. Mater.* **26**, 6941–6946 (2014).

52. Gassenq, A. et al. Raman spectral shift versus strain and composition in GeSn layers with 6%–15% sn content. *Appl. Phys. Lett.* **110**, 112101 (2017).

53. Prucnal, S. et al. Strain and band-gap engineering in Ge-Sn alloys via p doping. *Phys. Rev. Appl.* **10**, 064055 (2018).

54. Zidi, N., Chaouchi, A., D'Astorg, S., Rguiti, M. & Courtois, C. Impedance spectroscopy study on lead-free piezoelectric ceramics. *Bull. Mater. Sci.* **38**, 731–737 (2015).

55. Behera, B., Nayak, P. & Choudhary, R. N. P. Impedance spectroscopy study of NaBa2V5O15 ceramic. *J. Alloys Compd.* **436**, 226–232 (2007).

56. Sinclair, D. C., Adams, T. B., Morrison, F. D. & West, A. R. CaCu₂Ti₄O₁₂: one-step internal barrier layer capacitor. *Appl. Phys. Lett.* **80**, 2153–2155 (2002).

57. You, Y.-H. et al. Impedance spectroscopy characterization of resistance switching NiO thin films prepared through atomic layer deposition. *Appl. Phys. Lett.* **89**, 222105 (2006).

58. Kovaleva, N. N. et al. Bismuth layer properties in the ultrathin Bi–FeNi multi-layer films probed by spectroscopic ellipsometry. *Appl. Phys. Lett.* **119**, 183101 (2021).

59. Kusmartsev, F. V. Application of catastrophe theory to molecules and solitons. *Phys. Rep.* **183**, 1–35 (1989).

60. Miao, M. S. et al. Polarization-driven topological insulator transition in a GaN/InN/GaN quantum well. *Phys. Rev. Lett.* **109**, 186803 (2012).

61. Novoselov, K. S. et al. Electric field effect in atomically thin carbon films. *Science* **306**, 666–669 (2004).

62. Trabelsi, A. B. G. et al. Charged nano-domes and bubbles in epitaxial graphene. *Nanotechnology* **25**, 165704 (2014).

63. Trabelsi, A. B. G. et al. The emergence of quantum capacitance in epitaxial gra-phene. *J. Mater. Chem. C* . **4**, 5829–5838 (2016).

64. Trabelsi, A. B. G. et al. Morphological imperfections of epitaxial graphene: from a hindrance to the generation of new photo-responses in the visible domain. *Nanoscale* **9**, 11463–11474 (2017).

65. Trabelsi, A. B. G., Ouerghi, A., Kusmartseva, O. E., Kusmartsev, F. V. & Oueslati, M. Raman spectroscopy of four epitaxial graphene layers: macro-island grown on 4H-SiC 0001⁻ substrate and an associated strain distribution. *Thin Solid Films* **539**, 377–383 (2013).

66. Ben Gouider Trabelsi, A. et al. Raman spectroscopy imaging of exceptional electronic properties in epitaxial graphene grown on sic. *Nanomaterials* **10**, 2234 (2020).

67. Bkakri, R., Kusmartseva, O. E., Kusmartsev, F. V., Song, M. O. & Bouazizi, A. Degree of phase separation effects on the charge transfer properties of P3HT: graphene nanocomposites. *J. Lumin.* **161**, 264–270 (2015).

68. Bkakri, R. et al. Effects of the graphene content on the conversion efficiency of P3HT: graphene based organic solar cells. *J. Phys. Chem. Solids* **85**, 206–211 (2015).

69. Tan, S. et al. Interface-induced superconductivity and strain-dependent spin density waves in FeSe/SrTiO₃ thin films. *Nat. Mater.* **12**, 634–640 (2013).

70. Liu, D. et al. Electronic origin of high-temperature superconductivity in single-layer FeSe superconductor. *Nat. Commun.* **3**, 1–6 (2012).

71. He, S. et al. Phase diagram and electronic indication of high-temperature superconductivity at 65 K in single-layer FeSe films. *Nat. Mater.* **12**, 605–610 (2013).

72. Mermin, N. D. & Wagner, H. Absence of ferromagnetism or antiferromagnetism in one-or two-dimensional isotropic Heisenberg models. *Phys. Rev. Lett.* **17**, 1133 (1966).

73. Liu, Y. et al. Snake states and their symmetries in graphene. *Phys. Rev. B* **92**, 235438 (2015).

74. Kopnin, N. B., Heikkilä, T. T. & Volovik, G. E. High-temperature surface super-conductivity in topological flat-band systems. *Phys. Rev. B* **83**, 220503 (2011).

75. Giannozzi, P. et al. Quantum espresso: a modular and open-source software project for quantum simulations of materials. *J. Phys.: Condens. matter* **21**, 395502 (2009).

76. Perdew, J. P., Burke, K. & Ernzerhof, M. Generalized gradient approximation made simple. *Phys. Rev. Lett.* **77**, 3865 (1996).

77. Dal Corso, A. & Mosca Conte, A. Spin-orbit coupling with ultrasoft pseudopo-tentials: application to Au and Pt. *Phys. Rev. B* **71**, 115106 (2015).

78. Mosca Conte, A., Fabris, S. & Baroni, S. Properties of Pt-supported Co nano-magnets from relativistic density functional theory calculations. *Phys. Rev. B* **78**, 014416 (2008).

79. Fu, L. & Kane, C. L. Time reversal polarization and a Z₂ adiabatic spin pump. *Phys. Rev. B* **74**, 195312 (2006).

80. Gresch, D. et al. Z2Pack: numerical implementation of hybrid Wannier centers for identifying topological materials. *Phys. Rev. B* **95**, 075146 (2017).

81. Soluyanov, A. A. & Vanderbilt, D. Computing topological invariants without inversion symmetry. *Phys. Rev. B* **83**, 235401 (2011).

82. Djawad, Y. A., Kiely, J., Wraith, P. & Luxton, R. Lock-in amplifier as a sensitive instrument for biomedical measurement: analysis and implementation. *Indones. J. Electr. Eng. Comput. Sci.* **12**, 7214–7222 (2014).

83. Fafilek, G. & Breiter, M. W. Instrumentation for AC four-probe measurements of large impedances. *J. Electroanal. Chem.* **430**, 269–278 (1997).

AUTHOR CONTRIBUTIONS

B.Z. and D.G. contributed equally to this work and should be considered "co-first authors". A.K., F.V.K. and O.P. conceived the idea. A.M.C., O.P. and D.G. performed the DFT ab-initio calculations. B.Z. fabricated the samples and conducted optical and SEM measurements. A.K. performed Raman spectroscopy and impedance spectroscopy experiments and analysis. A.M.C, A.K., Y.Liu, O.P. and F.V.K. performed data analysis and developed optical theory. F.V.K. developed the $\mathbf{k} \cdot \mathbf{p}$ -theory model for the interpretation of ab-initio results and coordinated the experimental work. D.G. performed the calculation of the $\mathbb{Z}_2$ topological invariant. O.P. coordinated the theoretical ab-initio work. F.V.K., Y.Luo and O.P. supervised the project. A.M.C, O.P. A.K., D.G. and F.V.K. wrote the manuscript with input from B.Z. and Y.Liu. All authors contributed to the discussions.

COMPETING INTERESTS

The authors declare no competing interests.

ADDITIONAL INFORMATION

Supplementary information The online version contains supplementary material available at https://doi.org/10.1038/s41699-023-00381-5.

Correspondence and requests for materials should be addressed to Davide Grassano or Anna Kusmartseva.

Reprints and permission information is available at http://www.nature.com/reprints

Publisher's note Springer Nature remains neutral with regard to jurisdictional claims in published maps and institutional affiliations.

Published in partnership with FCT NOVA with the support of E-MRS